

## Supporting information for

### **The unevenness of the North Iberian crustal root, a snapshot of an elusive stage in margin reactivation.**

Gabriela Fernández-Viejo<sup>1</sup>, Patricia Cadenas<sup>2</sup>, Jorge Acevedo<sup>1</sup> and Sergio Llana-Fúnez<sup>1</sup>

<sup>1</sup>*Dept. Geology, University of Oviedo. Jesús Arias de Velasco s/n 33005 Oviedo, Spain*

<sup>2</sup>*ICM, CSIC, Passeig Marítim de la Barceloneta, 37-49, 08003, Barcelona*

#### **Contents of this file**

Text S1

Figures S1 and S2

Table S1

#### **Text S1. Crustal thickness from ambient seismic noise autocorrelation**

Autocorrelations of ambient seismic noise can be used to image lithospheric discontinuities below single seismic stations. The strategies to calculate this autocorrelations are quite diverse and different processing of data is applied in accordance with the dataset characteristics. The main differences are the length of the time windows to autocorrelate, the pre- and/or post-correlation time or frequency normalization and the limits of the applied band-pass filter (Becker and Knapmeyer-Endrun 2018; Andrés et al. 2020). Our processing workflow follows the ambient noise cross-correlation procedure of Bensen *et al.*, (2007) with several modifications based on the tests performed by Romero and Schimmel, (2018). Overall, it can be divided in four stages: preprocessing, construction of the stacked autocorrelograms (ACs), quality control and crustal depth determination. Here we show an example of AC calculation for station LIEG (Fig. S1).

#### **1) Pre-processing**

Vertical component data were downsampled to 25 Hz and cut into non-overlapping 3-hour fragments. Then the mean, the trend and the instrument response were removed. A crucial step is the application of a zero-phase band-pass filter to enhance the frequency band at which we expect to found the target information. In general, higher frequencies are used to extract the shallow subsurface response (e.g. 3-12 Hz in Romero and Schimmel, 2018), whereas lower frequency bands are employed to resolve deeper discontinuities. After several tests with different frequency bands, we found that the 2-4 Hz range

recovered the main reflections and showed a good daily consistency (Fig. S2A). This frequency band has also been used in other autocorrelation studies (e.g. Gorvatov *et al.*, 2013; Kennett *et al.*, 2015; Romero and Schimmel, 2018).

## **2) Construction of the stacked autocorrelograms**

We calculated the ACs using the phase cross-correlation (PCC) technique of Schimmel, (1999). This method is amplitude unbiased, which effectively avoids the necessity of applying a time or spectral normalization that may deteriorate the waveforms. The phase AC were computed for each 3-hour fragments with 25 s time lags and stacked using the time-frequency phase weighted stack (Schimmel and Gallart, 2007), a linear stacking procedure that enhances coherent arrivals and attenuates incoherent signals. The final ACs are obtained from the stacking of all the individual 3-hour autocorrelograms. 3-hour segments from the same day have also been stacked to create daily Acs, which are useful for testing the performance of the method.

## **3) Quality control**

The quality of the final ACs has been tested in three steps. First, the stability at different frequency bands was investigated and coherent reflectors have been observed (Fig. S2B). Next, stacks of randomly selected sets of 60, 90, 120 and all the available daily ACs have been computed in order to assess their temporal consistency and check if coherent arrivals can be identified. As shown in Fig. S2B, Moho related reflectors can be retrieved using as less as ~2 month of data, a much lower number than the one used in this work. Finally, daily autocorrelation plots (Fig. S2C) facilitate the recognition of anomalous signals that can be removed from the calculations.

## **4) Crustal depth determination**

In order to determine the Moho depth, the lag time of the maximum amplitude of the crust-mantle boundary originated reflection (Tibuleac and von Seggern, 2012) is picked in the autocorrelograms. However, due to the presence of several reflections, the unique identification of this specific signal can be problematic. To reduce this uncertainty, we applied the automatic approach of Becker and Knapmeyer-Endrun (2018) with a few modifications. This method begins with the filtering of the stacked autocorrelograms between 2 and 4 Hz with a four-order Butterworth filter (Fig. S2D). Next, the second derivative of the envelope of the resulting AC signal is calculated. Finally, an amplitude normalization using an automatic gain control is performed to emphasize the amplitude variations of the signal (Fig. S2D). The greatest changes are linked to the largest fluctuations in the slope of the envelope. At this

point, Becker and Knapmeyer-Endrun (2018) select the local maxima of the second derivative within a time window for expected Moho reflections based on prior information from the study area. However, we have observed that picking the local minima instead of the local maxima yields better results for our datasets, because it tends to correlate with the maximum amplitude of an identifiable reflectivity change in the autocorrelogram's waveform (Fig. S2D).

Our lag time windows for retrieving Moho reflections are based on the crustal thickness maps derived from deep seismic sounding studies and receiver function determinations (Table S1, Diaz *et al.*, 2016) plus a  $\pm 1.5$  s lag time uncertainty (Fig. S2D). Considering the large differences between the crust-mantle boundary topography obtained from each of these techniques, up to 15 km below the Cantabrian Mountains, time windows for each station are long enough to ensure that the selected Moho lag time is picked with a sufficient degree of freedom. Lag times, which are expressed in two-way-time, are converted to depth using an average crustal P-wave velocity of 6 km/s based on  $V_p$  velocities obtained in refraction profiles through the study area by Fernández-Viejo *et al.* (2000). The P-wave velocity for depth conversion can be a source of error in the measurements, so it is recommended to assume a 5% velocity uncertainty. In practice, this results in an average error of  $\pm 2.1$  km for the Moho depth determinations (Table S1).

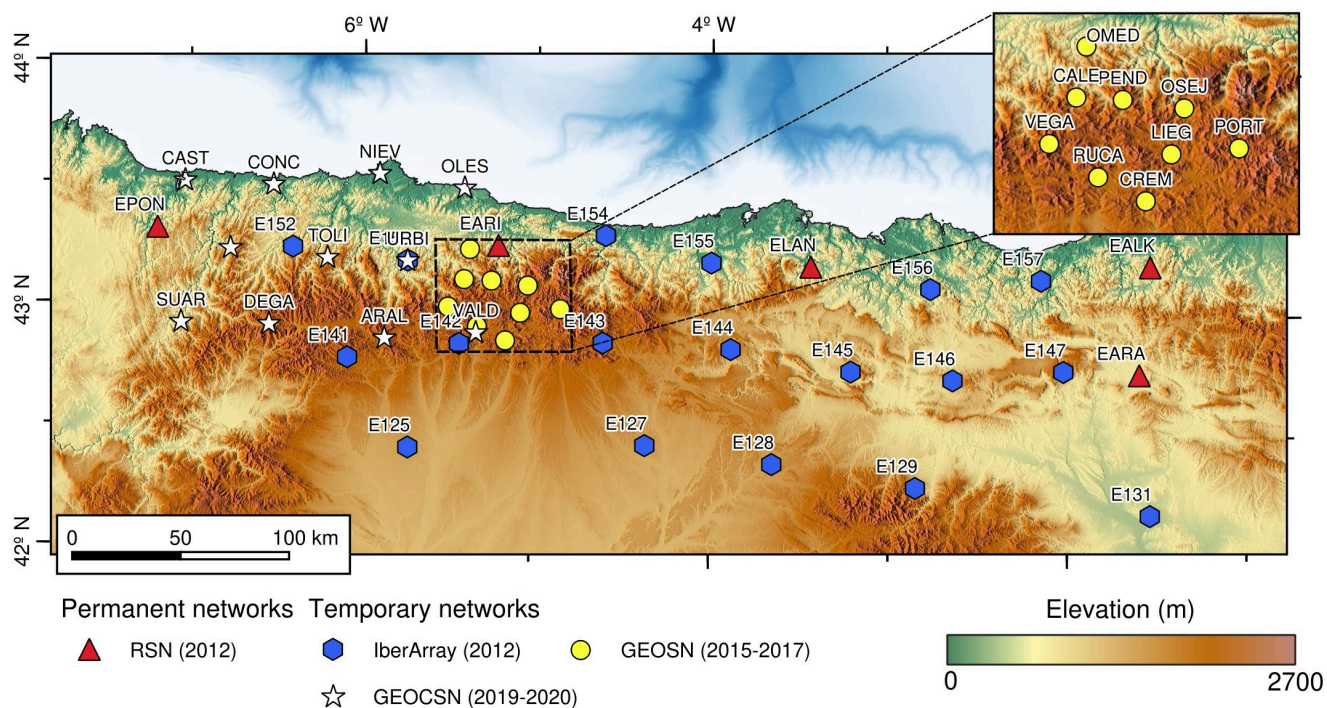


**Figure S1.** Topographic map showing the location of the permanent seismic stations of the Spanish Seismological Network (RSN) and the portable stations belonging to the IberArray, GEOSN (Geocantábrica Seismic Network) and GEOCSN (Geocantábrica-Costa Seismic Network) temporary experiments.

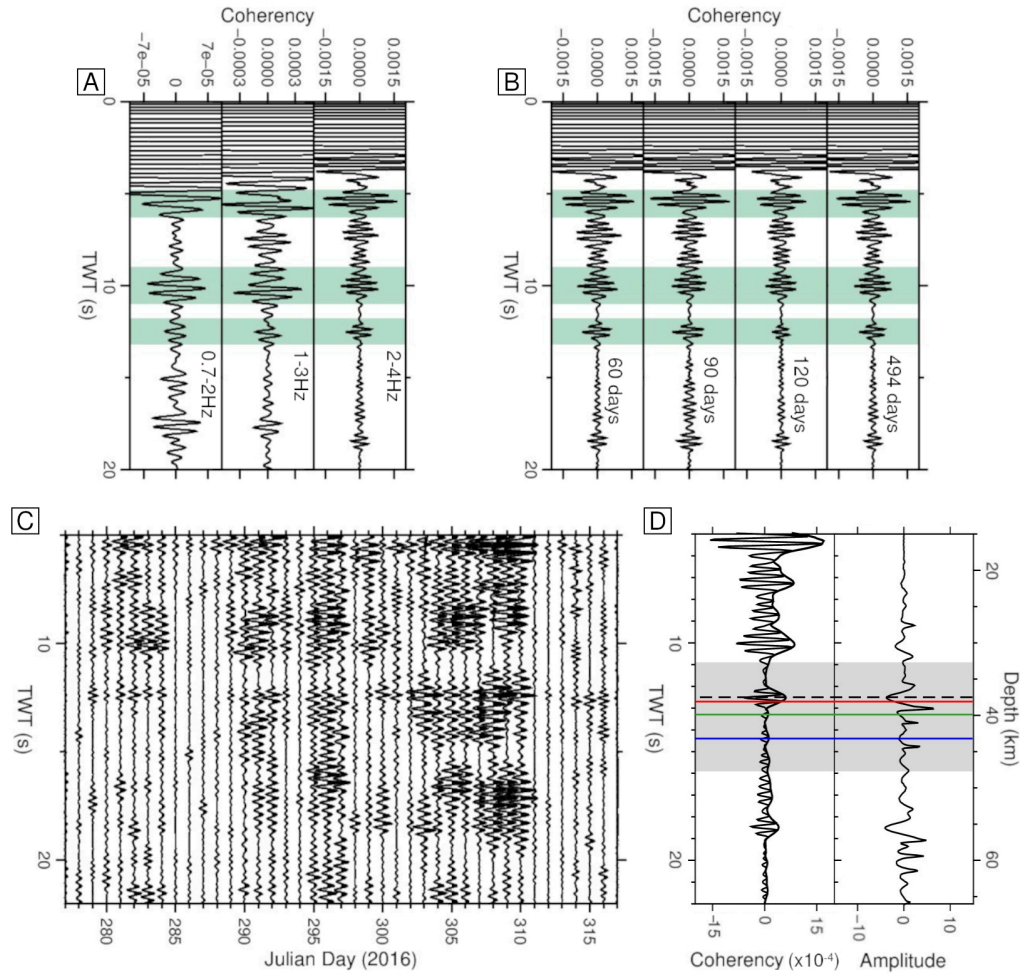


**Figure S2.** Quality tests and crustal depth determination for station LIEG (Location in Figure S1). A) Example of autocorrelogram stacks computed at frequency bands between 0.7-2Hz (left), 1-3Hz (center) and 2-4Hz (right). Green rectangles highlight coherent identified reflections. TWT: two-way-time. B) Sequential stacks of 60, 90 120 and 494 daily autocorrelograms. Note how the same reflections of Fig. S1a (green surfaces) are retrieved. C) Daily autocorrelation section showing a consistent reflection at  $\sim 12.5$  s. D) Automatic picking of the Moho lag time by selecting the local minima of the second derivative of the envelope (right) of the total autocorrelogram stack (left). Note how this minima coincides with the maximum amplitude of a coherent reflection that can also be observed in the daily autocorrelation section. The grey surface represents the expected time window for Moho reflections based on the calculated lag times from previous receiver function (RF, red) and seismic data (R/WAR, blue) determinations (Table S1, Díaz et al, 2016) extended with a  $\pm 1.5$ s lag time uncertainty.

**Table S1.** Overview of Moho depths from ACs and R/WAR. Moho depths obtained by Díaz *et al.* (2016) from receiver functions (RF) and R/WAR used to determine AC lag time windows. Lag times

corresponding to Moho depths are shown in brackets. They are expressed in two-way-time and calculated using  $V_p=6$  km/s.

Network	Station	Díaz <i>et al.</i> 2016		This study		
		Moho depth RF (km)	Moho depth R/WAR (km)	Moho depth R/WAR (km)	Moho depth AC (km)	AC Moho depth error $\pm$ (km)
GEOSN	CALE	35 (11.7)	42 (14)	45.2 (15.1)	43.5 (14.5)	2.18
GEOSN	CREM	37 (12.3)	40 (13.3)	38 (12.7)	37.8 (12.6)	1.89
GEOSN	LIEG	38 (12.7)	43 (14.3)	40 (13.3)	37.6 (12.5)	1.88
GEOSN	OMED	35 (11.7)	48 (16)	48.5 (16.2)	44.6 (14.9)	2.23
GEOSN	OSEJ	39 (13)	49 (16.3)	44.2 (14.7)	39.2 (13.1)	1.96
GEOSN	PEND	35 (11.7)	49 (16.3)	46 (15.3)	47.5 (15.8)	2.38
GEOSN	PORT	39 (13)	48 (16)	43.7 (14.6)	47.6 (15.9)	2.38
GEOSN	RUCA	35 (11.7)	39 (13)	38.8 (12.9)	38.1 (12.7)	1.91
GEOSN	VEGA	35 (11.7)	39 (13)	39.7 (13.2)	41.4 (13.8)	2.07
GEOCSN	CAST	29 (9.7)	27 (9)	30.1 (10)	25 (8.3)	1.25
GEOCSN	CONC	33 (11)	30 (10)	29.8 (9.9)	32.7 (10.9)	1.64
GEOCSN	NIEV	33 (11)	36 (12)	36.8 (12.3)	33.3 (11.1)	1.67
GEOCSN	OLES	35 (11.7)	46 (15.3)	46.5 (15.5)	39.8 (13.3)	1.99
GEOCSN	LAGO	33 (11)	30 (10)	29.7 (9.9)	33.5 (11.2)	1.68
GEOCSN	TOLI	35 (11.7)	34 (11.3)	32.1 (10.7)	36.6 (12.2)	1.83
GEOCSN	URBI	33 (11)	38 (12.7)	39.7 (13.2)	37.8 (12.6)	1.89
GEOCSN	SUAR	30 (10)	34 (11.3)	33.3 (11.1)	33.9 (11.3)	1.7
GEOCSN	DEGA	34 (11.3)	35 (11.7)	33 (11)	32.1 (10.7)	1.61
GEOCSN	ARAL	38 (12.7)	35 (11.7)	34.3 (11.4)	41.4 (13.8)	2.07
GEOCSN	VALD	38 (12.7)	40 (13.3)	38.2 (12.7)	36.9 (12.3)	1.85
RSN	EARI	36 (12)	49 (16.3)	49.4 (16.5)	48.3 (16.1)	2.42
RSN	EPON	26 (8.7)	30 (10)	29.5 (9.8)	32.1 (10.7)	1.61
RSN	ELAN	49 (16.3)	42 (14)	41.1 (13.7)	43.1 (14.4)	2.16
RSN	EALK	44 (14.7)	30 (10)	-	39.3 (13.1)	1.97
RSN	EARA	41 (13.7)	46 (15.3)	42 (14)	47.2 (15.7)	2.36
IberArray	E152	35 (11.7)	35 (11.7)	31.2 (10.4)	36.3 (12.1)	1.8
IberArray	E153	33 (11)	38 (12.7)	39.7 (13.2)	36.2 (12.1)	1.82
IberArray	E154	35 (11.7)	49 (16.3)	49.1 (16.4)	45.8 (15.3)	2.29
IberArray	E155	40 (13.3)	42 (14)	41.2 (13.7)	38.7 (12.9)	1.94
IberArray	E156	38 (12.7)	46 (15.3)	44 (14.7)	39.1 (13)	1.96
IberArray	E157	42 (14)	39 (13)	50.6 (16.9)	38.1 (12.7)	1.91

IberArray	E141	38 (12.7)	35 (11.7)	33.9 (11.3)	40.5 (13.5)	2.03
IberArray	E142	34 (11.3)	38 (12.7)	36.4 (12.1)	38.2 (12.7)	1.91
IberArray	E143	31 (10.3)	40 (13.3)	37.7 (12.6)	41.4 (13.8)	2.07
IberArray	E144	37 (12.3)	38 (12.7)	34.5 (11.5)	37.2 (12.4)	1.86
IberArray	E145	38 (12.7)	40 (13.3)	35.7 (11.9)	41 (13.7)	2.05
IberArray	E146	40 (13.3)	43 (14.3)	41.8 (13.9)	44.5 (14.8)	2.23
IberArray	E147	43 (14.3)	45 (15)	42.1 (14)	44.7 (14.9)	2.24
IberArray	E125	32 (10.7)	38 (12.7)	33 (11)	29.5 (9.8)	1.48
IberArray	E127	34 (11.3)	38 (12.7)	33.9 (11.3)	34.2 (11.4)	1.71
IberArray	E128	37 (12.3)	33 (11)	36.3 (12.1)	31.5 (10.5)	1.58
IberArray	E129	39 (13)	40 (13.3)	40.6 (13.5)	36.9 (12.3)	1.85
IberArray	E131	33 (11)	37 (12.3)	-	31.8 (10.6)	1.59

## REFERENCES

- Andrés, J., Ayarza, P., Schimmel, M., Palomeras, I., Ruiz, M., and Carbonell, R., 2020, What can seismic noise tell us about the Alpine reactivation of the Iberian Massif? An example in the Iberian Central System. *Solid Earth*, v. 11(6), p. 2499-2513, doi: 10.5194/se-11-2499-2020
- Becker, G. and Knapmeyer-Endrun, B., 2018, Crustal thickness across the Trans-European Suture Zone from ambient noise autocorrelations: *Geophysical Journal International*, v. 212, p. 1237–1254, doi: 10.1093/gji/ggx485
- Bensen, G.D., Ritzwoller, M.H., Barmin, M.P., Levshin, A.L., Lin, F., Moschetti, M.P., Shapiro, N.M. and Yang, Y., 2007, Processing seismic ambient noise data to obtain reliable broad-band surface wave dispersion measurements: *Geophysical Journal International*, v. 169, p. 1239-1260, doi: 10.1111/j.1365-246X.2007.03374.x
- Diaz, J., Gallart, J. and Carbonell, R., 2016, Moho topography beneath the Iberian-Western Mediterranean region mapped from controlled-source and natural seismicity surveys: *Tectonophysics*, v. 692, p. 74-85, doi: 10.1016/j.tecto.2016.08.023

- Fernández-Viejo, G., Gallart, J., Pulgar, J.A., Córdoba, D. and Dañobeitia, J.J., 2000, Seismic signature of Variscan and Alpine tectonics in NW Iberia: Crustal structure of the Cantabrian Mountains and Duero basin: *Journal of Geophysical Research, Solid Earth*, v. 105, p. 3001-3018, doi: 10.1029/1999JB900321.
- Gorbatov, A., Saygin, E., & Kennett, B. L. N., 2013, Crustal properties from seismic station autocorrelograms. *Geophysical Journal International*, v. 192(2), p. 861-870, doi: 10.1093/gji/ggs064
- Kennett, B.L.N., Saygin, E. and Salmon, M., 2015, Stacking autocorrelograms to map Moho depth with high spatial resolution in southeastern Australia: *Geophysical Research Letters*, v. 42(18), p. 7490–7497, doi: 10.1002/2015GL065345
- Romero, P. and Schimmel, M., 2018, Mapping the basement of the Ebro basin in Spain with seismic ambient noise autocorrelations: *Journal of Geophysical Research-Solid Earth*, v. 123, p. 5052-5067, doi: 10.1029/2018JB015498
- Schimmel, M., 1999, Phase cross-correlations: design, comparisons and applications: *Bulletin of the Seismological Society of America*, v. 89(5), p. 1366–1378.
- Schimmel, M. and Gallart, J., 2007, Frequency-dependent phase coherence for noise suppression in seismic array data: *Journal of Geophysical Research*, v. 112, B04303, doi: 10.1029/2006JB004680.
- Tibuleac, I.M. and von Seggern, D., 2012, Crust-mantle boundary reflectors in Nevada from ambient seismic noise autocorrelations: *Geophysical Journal International*, v. 189, p. 493–500, doi: 10.1111/j.1365-246X.2011.05336.x